Fundamental limits of measuring single-molecule rotational mobility

Oumeng Zhang, Matthew D. Lew

Oumeng Zhang, Matthew D. Lew, "Fundamental limits of measuring single-molecule rotational mobility," Proc. SPIE 10884, Single Molecule Spectroscopy and Superresolution Imaging XII, 1088412 (22 February 2019); doi: 10.1117/12.2506712

SPIE.

Event: SPIE BiOS, 2019, San Francisco, California, United States

Fundamental Limits of Measuring Single-Molecule Rotational Mobility

Oumeng Zhang[a] and Matthew D. Lew*[a]

[a]Department of Electrical and Systems Engineering, Washington University in St. Louis, 1 Brookings Drive, St. Louis, MO, USA 63130

ABSTRACT

Various methods exist for measuring molecular orientation, thereby providing insight into biochemical activities at nanoscale. Since fluorescence intensity and not electric field is detected, these methods are limited to measuring even-order moments of molecular orientation. However, any measurement noise, for example photon shot noise, will result in nonzero measurements of any of these even-order moments, thereby causing rotationally-free molecules to appear to be partially constrained. Here, we build a model to quantify measurement errors in rotational mobility. Our theoretical framework enables scientists to choose the optimal single-molecule orientation measurement technique for any desired measurement accuracy and photon budget.

Keywords: single-molecule fluorescence imaging, orientational dynamics, measurement bias, photon shot noise

1. INTRODUCTION

Since single molecules were first observed almost 30 years ago,[1] their rotational dynamics have been used to reveal the nanoscale organization of DNA[2–4] and the movement of molecular motors.[5–9] To discern molecular rotation, the fluorescence emitted by single molecules can be phase-modulated, detected after polarization filtering, and/or measured in response to the polarization of the excitation light.[10] Since fluorescence intensity and not electric field is detected, these methods are limited to measuring even-order moments of the molecular orientation, regardless of the angle between absorption and emission dipole moments of the molecule.[11] A signature of rotationally-free molecules is the vanishing of specific orientational second-order moments. However, any measurement noise, for example photon shot noise, will result in nonzero measurements of any of the aforementioned even-order moments, thereby causing rotationally-free molecules to appear to be partially constrained.

Here, we evaluate the bias in rotational constraint estimation for three orientation measurement strategies, including three-dimensional orientation measurements using point spread function engineering and in-plane (2D) orientation measurements using excitation polarization modulation. Our approach can be readily adapted to analyze any orientation-measurement methods, thereby enables scientists to evaluate and choose the optimal single-molecule orientation measurement technique.

2. FORWARD IMAGING MODEL

A single fluorescent molecule is modeled as an oscillating electric dipole with an instantaneous orientation $\boldsymbol{\mu} = [\mu_x, \mu_y, \mu_z]^\dagger$ in 3D. Its normalized projection in the xy plane is denoted by $\boldsymbol{\zeta} = [\zeta_x, \zeta_y]^\dagger = [\mu_x, \mu_y]/\sqrt{\mu_x^2 + \mu_y^2}$. Here, we derive the forward imaging model for both absorption- and emission-based methods.

*mdlew@wustl.edu; phone 1-314-935-6790; fax 1-314-935-7500; lewlab.wustl.edu

Single Molecule Spectroscopy and Superresolution Imaging XII, edited by Zygmunt Karol Gryczynski, Ingo Gregor, Felix Koberling, Proc. of SPIE Vol. 10884, 1088412 · © 2019 SPIE
CCC code: 1605-7422/19/$18 · doi: 10.1117/12.2506712

2.1 In-Plane Excitation Modulation

Three distinct in-(xy) plane excitation polarizations $\boldsymbol{E}_k = [E_{x,k}, E_{y,k}]^\dagger, k = \{1,2,3\}$ are used to excite the molecule. Since the number of detected photons from the molecule is proportional to its absorption probability, the photons collected g_k under each excitation polarization are given by[4]

$$\begin{bmatrix} g_1 \\ g_2 \\ g_3 \end{bmatrix} = s \begin{bmatrix} |E_{x,1}|^2 & |E_{y,1}|^2 & 2\mathcal{R}\{E_{x,1}E_{y,1}\} \\ |E_{x,2}|^2 & |E_{y,2}|^2 & 2\mathcal{R}\{E_{x,2}E_{y,2}\} \\ |E_{x,3}|^2 & |E_{y,3}|^2 & 2\mathcal{R}\{E_{x,3}E_{y,3}\} \end{bmatrix} \begin{bmatrix} \langle \zeta_x^2 \rangle \\ \langle \zeta_y^2 \rangle \\ \langle \zeta_x \zeta_y \rangle \end{bmatrix} + \begin{bmatrix} b_1 \\ b_2 \\ b_3 \end{bmatrix} = s[\boldsymbol{B}_{xx}, \boldsymbol{B}_{yy}, \boldsymbol{B}_{xy}] \begin{bmatrix} \langle \zeta_x^2 \rangle \\ \langle \zeta_y^2 \rangle \\ \langle \zeta_x \zeta_y \rangle \end{bmatrix} + \begin{bmatrix} b_1 \\ b_2 \\ b_3 \end{bmatrix}, \quad (1)$$

where s is a brightness scaling factor, namely the total photons detected from the emitter, and $\boldsymbol{b}$ represents the background photons. Angled brackets $\langle \cdot \rangle$ represent the temporal average over one camera frame. Vectors $\boldsymbol{B}_{ij}$ are termed the basis images of the imaging system,[12] which represent the measured intensity distributions collected from a molecule exhibiting molecular second-order moments $\langle \zeta_i \zeta_j \rangle$.

2.2 Standard Point Spread Function and Tri-spot Point Spread Function

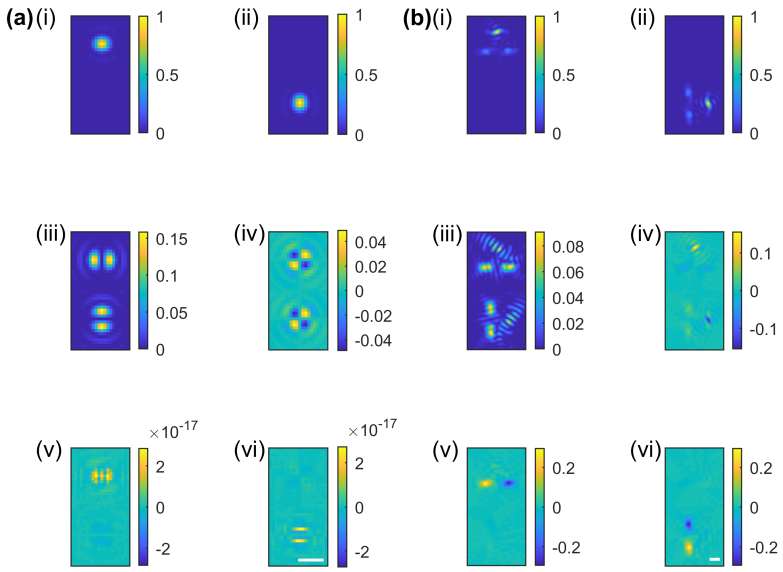

Figure 1. Basis images of (a) the standard PSF and (b) the Tri-spot PSF. (i)-(vi) represent the basis images $\boldsymbol{B}_{xx}$, $\boldsymbol{B}_{yy}$, $\boldsymbol{B}_{zz}$, $\boldsymbol{B}_{xy}$, $\boldsymbol{B}_{xz}$, $\boldsymbol{B}_{yz}$, respectively. Top and bottom half of each basis image represent x- and y-polarized images, respectively, which can be separated using a polarization beam splitter in the emission path of a fluorescence microscope. Colorbar: normalized intensity. Scale bar: 500 nm.

Similar to the excitation-modulation method, the image captured by a detector from a dipole emitter is given by[12–16]

$$\boldsymbol{g} = s[\boldsymbol{B}_{xx}, \boldsymbol{B}_{yy}, \boldsymbol{B}_{zz}, \boldsymbol{B}_{xy}, \boldsymbol{B}_{xz}, \boldsymbol{B}_{yz}] \begin{bmatrix} \langle \mu_x^2 \rangle \\ \langle \mu_y^2 \rangle \\ \langle \mu_z^2 \rangle \\ \langle \mu_x \mu_y \rangle \\ \langle \mu_x \mu_z \rangle \\ \langle \mu_y \mu_z \rangle \end{bmatrix} + \boldsymbol{b}, \quad (2)$$

where $\boldsymbol{B}_{ij}$ are the basis images corresponding to the orientational second-order moments $\langle \mu_i \mu_j \rangle$. The basis images can be computed based on a vectorial diffraction model for any given imaging system.[12] Certain methods

are sensitive to a subset of the second moments, e.g., the standard point spread function (PSF, Fig. 1(a)),[17] while some methods can measure all second moments, e.g., the Tri-spot PSF (Fig. 1(b)).[18]

3. BIAS IN ROTATIONAL CONSTRAINT

3.1 2D Rotational Constraint Measured using Excitation Modulation

We rearrange the second moments obtained by inverting Eq. (1) into a 2-by-2 Hermitian matrix and perform eigendecomposition as

$$\boldsymbol{M}_{2\mathrm{D}} = \begin{bmatrix} \langle \zeta_x^2 \rangle & \langle \zeta_x \zeta_y \rangle \\ \langle \zeta_x \zeta_y \rangle & \langle \zeta_y^2 \rangle \end{bmatrix} = (2\lambda_1 - 1)\boldsymbol{\nu}_1 \boldsymbol{\nu}_1^\dagger + (2 - 2\lambda_1)\frac{\boldsymbol{I}}{2} = \gamma_{2\mathrm{D}} \boldsymbol{\nu}_1 \boldsymbol{\nu}_1^\dagger + (1 - \gamma_{2\mathrm{D}})\frac{\boldsymbol{I}}{2}, \tag{3}$$

where λ_i and $\boldsymbol{\nu}_i$ are the eigenvalues and eigenvectors of $\boldsymbol{M}_{2\mathrm{D}}$. The matrix $\boldsymbol{M}_{2\mathrm{D}}$ can be viewed as a superposition of a fixed molecule with orientation $\boldsymbol{\nu}_1$, and a freely-rotating molecule (i.e., an isotropic emitter). The rotational constraint γ_{2D} is therefore defined as the immobile fraction in $\boldsymbol{M}_{2\mathrm{D}}$, where $\gamma_{2D} = 0$ represents a freely-rotating molecule, and $\gamma_{2D} = 1$ represents an immobile molecule.

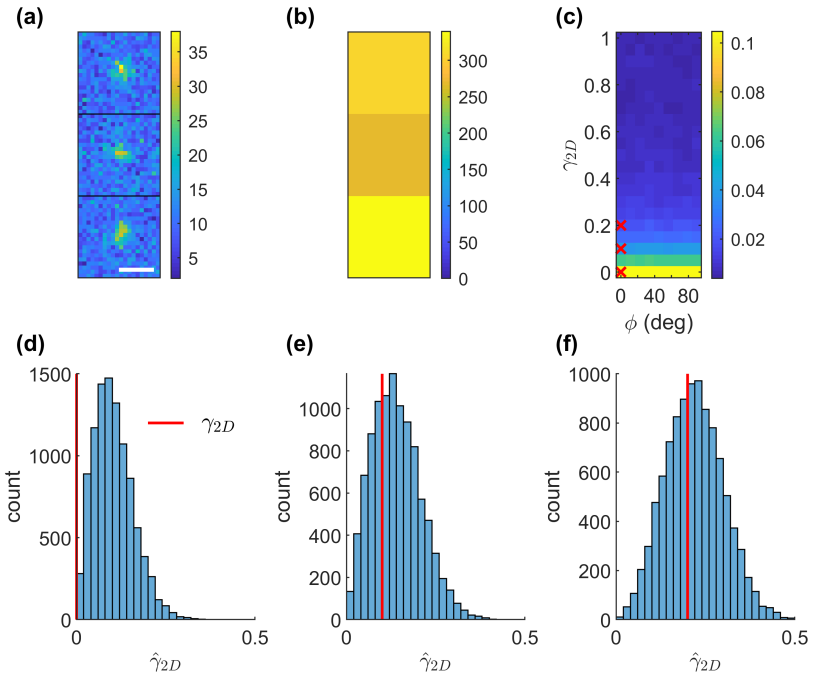

Figure 2. (a) One simulated measurement consists of three images of a freely-rotating emitter under excitation polarizations $\boldsymbol{E}_k = [\sin(2\pi k/3), \cos(2\pi k/3)]^\dagger$, $k = \{1, 2, 3\}$ under 1000 signal photons and 10 background photons per 58.5×58.5 nm^2. Scale bar: 500 nm. (b) Integrated photons g_k in each image after background subtraction. (c) Average bias in rotational constraint estimates $\hat{\gamma}_{2\mathrm{D}}$ using 10,000 simulated images for molecules with varying average azimuthal angles (in-plane orientations ϕ) and rotational constraints under the aforementioned SNR using the in-plane excitation modulation method. (d)-(f) The distribution of rotational constraint estimations for molecules with average orientations along the x-axis and ground-truth rotational constraints $\gamma_{2\mathrm{D}}$ of (d) 0, (e) 0.1, (f) 0.2 (vertical lines in (d)-(f) and crosses in (c)), respectively.

To show the bias in rotational constraint estimation, we simulate 10,000 images with Poisson noise under the signal of $s = 1000$ photons and background of $\boldsymbol{b} = [810, 810, 810]^\dagger$ photons (Fig. 2(a)) for molecules with varying in-plane orientations and rotational constraints. The three excitation polarizations are symmetric, i.e.,

$\boldsymbol{E}_k = [\sin(2\pi k/3), \cos(2\pi k/3)]^\dagger$. The basis-image matrix is

$$\boldsymbol{B}_{\text{exMod}} = [\boldsymbol{B}_{xx}, \boldsymbol{B}_{yy}, \boldsymbol{B}_{xy}] = \begin{bmatrix} 2/3 & 0 & 0 \\ 1/6 & 3/6 & \sqrt{3}/6 \\ 1/6 & 3/6 & -\sqrt{3}/6 \end{bmatrix}. \tag{4}$$

A 526.5×526.5 nm^2 box (∼3.5 FWHM of the standard PSF) is used to integrate photons captured in each camera frame, e.g., $\boldsymbol{g} = [g_1, g_2, g_3]^\dagger = [308, 268, 340]^\dagger$ in Fig. 2(b) for three simulated images (one measurement) of an isotropic emitter in Fig. 2(a). A basis inversion estimator is used to recover the second moments from the simulated images, e.g., $[\langle\hat{\zeta_x^2}\rangle, \langle\hat{\zeta_y^2}\rangle, \langle\hat{\zeta_x\zeta_y}\rangle]^\dagger = \boldsymbol{B}_{\text{exMod}}^{-1}\boldsymbol{g}/s = [0.5044, 0.4956, 0.0681]^\dagger$ for the aforementioned measurement. The apparent rotational constraint $\hat{\gamma}_{\text{2D}} = 0.1364$ given by Eq. (3) is nonzero due to the non-uniform $\boldsymbol{g}$.

The average bias (Fig. 2(c)) for molecules with average orientation along the x-axis and rotational constraint of $\gamma_{\text{2D}} = 0, 0.1, 0.2$ (Fig. 2(d-f)) are 0.1031, 0.0395, and 0.0188 ($\hat{\gamma}_{\text{2D}} = 0.1031$, 0.1395, and 0.2188). These constraints correspond to biases in cone half-angle of 8.55°, 2.97°, and 1.35°, respectively, if the molecule is symmetrically rotating in a cone.

3.2 3D Rotational Constraint Measured using Standard PSF

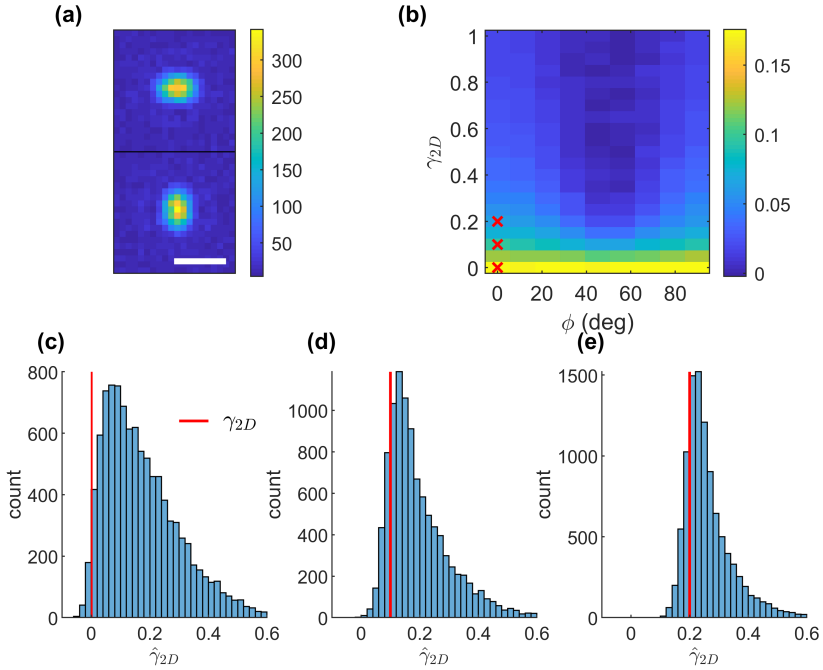

Figure 3. (a) One simulated image of a freely-rotating emitter using the standard PSF under 5000 signal photons and 10 background photons per 58.5×58.5 nm^2. Top: $x-$polarized image, bottom: y-polarized image. Scale bar: 500 nm. (b) Average bias in rotational constraint estimates $\hat{\gamma}_{\text{3D}}$ using 10,000 simulated images for molecules with varying average azimuthal angles (in-plane orientations ϕ) and rotational constraints under the aforementioned SNR using the standard PSF. (c)-(e) The distribution of rotational constraint estimations for molecules with average orientations along the x-axis and ground-truth rotational constraints γ_{2D} of (c) 0, (d) 0.1, (e) 0.2 (vertical lines in (c)-(e) and crosses in (b)), respectively.

Similar to the 2D second-moment matrix M_{2D}, we assemble a 3-by-3 Hermitian matrix from the second-

moment measurements obtained by inverting Eq. (2) and decompose it as

$$\boldsymbol{M}_{3\mathrm{D}} = \begin{bmatrix} \langle\mu_x^2\rangle & \langle\mu_x\mu_y\rangle & \langle\mu_x\mu_z\rangle \\ \langle\mu_x\mu_y\rangle & \langle\mu_y^2\rangle & \langle\mu_y\mu_z\rangle \\ \langle\mu_x\mu_z\rangle & \langle\mu_y\mu_z\rangle & \langle\mu_z^2\rangle \end{bmatrix} = \frac{3\lambda_1 - 1}{2}\boldsymbol{\nu}_1\boldsymbol{\nu}_1^\dagger + \frac{3 - 3\lambda_1}{2}\frac{\boldsymbol{I}}{3} + \frac{\lambda_2 - \lambda_3}{2}(\boldsymbol{\nu}_2\boldsymbol{\nu}_2^\dagger - \boldsymbol{\nu}_3\boldsymbol{\nu}_3^\dagger)$$
$$= \gamma_{3\mathrm{D}}\boldsymbol{\nu}_1\boldsymbol{\nu}_1^\dagger + (1 - \gamma_{3\mathrm{D}})\frac{\boldsymbol{I}}{3} + \boldsymbol{M}_{\mathrm{noise}}. \tag{5}$$

The matrix $\boldsymbol{M}_{3\mathrm{D}}$ can be viewed as a superposition of a fixed molecule with orientation $\boldsymbol{\nu}_1$, a freely-rotating molecule, and a noise component $\boldsymbol{M}_{\mathrm{noise}}$ that is orthogonal to $\boldsymbol{\nu}_1$. Due to the fact that the standard PSF has no sensitivity towards the out-of-plane second moments $\langle\mu_x\mu_z\rangle$ and $\langle\mu_y\mu_z\rangle$ (Fig. 1(a)(v,vi)), only the in-plane second moments are used to compute the rotational constraint

$$\hat{\gamma}_{3\mathrm{D}} = 1 - \frac{3}{2}\left(\langle\hat{\mu_x^2}\rangle + \langle\hat{\mu_y^2}\rangle - \sqrt{\left(\langle\hat{\mu_x^2}\rangle - \langle\hat{\mu_y^2}\rangle\right)^2 + \left(2\langle\hat{\mu_x\mu_y}\rangle\right)^2}\right). \tag{6}$$

We simulate molecules under 5000 signal photons and 10 background photons per 58.5×58.5 nm^2 (Fig. 3(a)), and use a pseudoinverse estimator (MMSE)[19] to recover the orientational second moments as

$$[\langle\hat{\mu_x^2}\rangle, \langle\hat{\mu_y^2}\rangle, \langle\hat{\mu_x^2}\rangle, \langle\hat{\mu_x\mu_y}\rangle]^\dagger = \boldsymbol{B}_{\mathrm{standard}}^{+}\boldsymbol{g}/s \tag{7}$$

where $\boldsymbol{B}_{\mathrm{standard}} = [\boldsymbol{B}_{xx}, \boldsymbol{B}_{yy}, \boldsymbol{B}_{zz}, \boldsymbol{B}_{xy}]$ is a N-by-4 matrix, and N represents the number of pixels sampled in the standard PSF. Superscript $(\cdot)^+$ represents the pseudoinverse.

The measured rotational constraints are biased similarly to the 2D excitation method. The average bias (Fig. 3(b)) for molecules with average orientation along the x-axis and rotational constraint of $\gamma_{3\mathrm{D}} = 0, 0.1, 0.2$ (Fig. 3(c-e)) are 0.1732, 0.0953, and 0.0635, which correspond to biases in cone half-angle of 15.80°, 7.65°, and 4.59°, respectively. One thing to note is that due to the different definitions of in-plane ($\gamma_{2\mathrm{D}}$) and 3D ($\gamma_{3\mathrm{D}}$) rotational constraints, these values cannot be directly compared to those using the excitation modulation method.

3.3 3D Rotational Constraint Measured using Tri-Spot PSF

For the Tri-spot PSF, the rotational constraint is quantified as a function of all six 3D second moments. Similarly to Section 3.2, we simulate molecules under 5000 signal photons and 10 background photons per 58.5×58.5 nm^2 (Fig. 4(a)), and use a similar pseudoinverse estimator to recover the orientational second moments as

$$[\langle\hat{\mu_x^2}\rangle, \langle\hat{\mu_y^2}\rangle, \langle\hat{\mu_x^2}\rangle, \langle\hat{\mu_x\mu_y}\rangle, \langle\hat{\mu_x\mu_z}\rangle, \langle\hat{\mu_y\mu_z}\rangle]^\dagger = \boldsymbol{B}_{\text{Tri-spot}}^{+}\boldsymbol{g}/s \tag{8}$$

where $\boldsymbol{B}_{\text{Tri-spot}} = [\boldsymbol{B}_{xx}, \boldsymbol{B}_{yy}, \boldsymbol{B}_{zz}, \boldsymbol{B}_{xy}, \boldsymbol{B}_{xz}, \boldsymbol{B}_{yz}]$ is a N-by-6 matrix, and N represents the number of pixels sampled in the Tri-spot PSF.

The average bias (Fig. 4(b)) for molecules with average orientation along the x-axis and rotational constraint of $\gamma_{3\mathrm{D}} = 0, 0.1, 0.2$ (Fig. 4(c-e)) are 0.1210, 0.0598, and 0.0393, which correspond to biases in cone half-angle of 11.62°, 4.92°, and 2.87°, respectively. The bias is smaller than that of the standard PSF. Further, distributions of measured rotational constraint $\gamma_{3\mathrm{D}}$ (Fig. 4(e)) are closer to Gaussian compared to those of the standard PSF (Fig. 3(e)), i.e., $\hat{\gamma}_{3\mathrm{D}}$ is more accurate when using the Tri-spot PSF. Note that these results are based on molecules with average orientations in the xy plane. Since the standard PSF has no sensitivity towards two of the out-of-plane second moments, its performance for out-of-plane molecules (not shown here) is worse compared to the in-plane case.

4. CONCLUSION

In this paper, we show that bias in measuring rotational constraint is unavoidable due to the limited SNR. This bias should be taken into consideration when interpreting orientation measurements using any fluorescence-based method. We simulated the performance of three orientation measurement methods, in-plane excitation modulation, the standard PSF, and the Tri-spot PSF, and quantified their performance based on the bias in

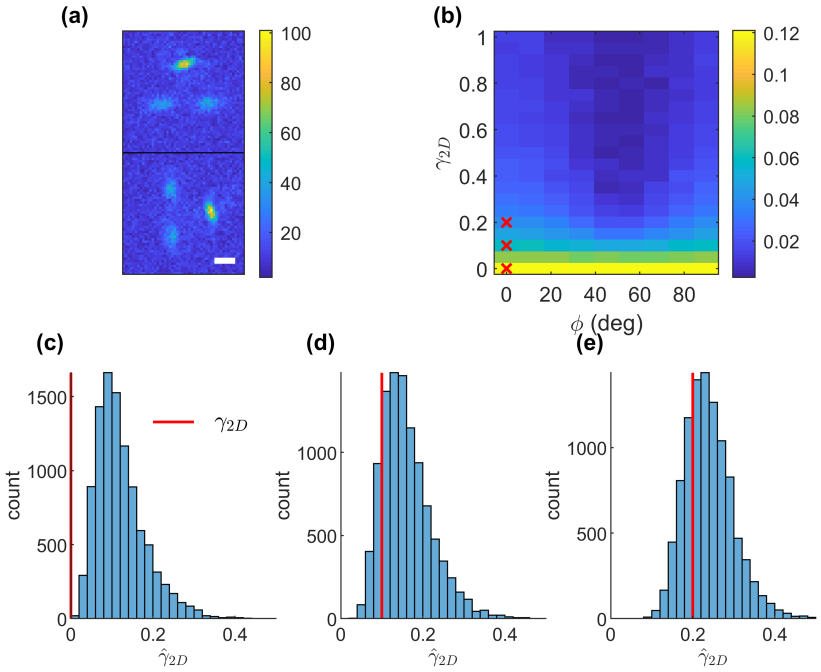

Figure 4. (a) One simulated image of a freely-rotating emitter using the Tri-spot PSF under 5000 signal photons and 10 background photons per 58.5×58.5 nm^2. Top: $x-$polarized image, bottom: y-polarized image. Scale bar: 500 nm. (b) Average bias in rotational constraint estimates $\hat{\gamma}_{3D}$ using 10,000 simulated images for molecules with varying average azimuthal angles (in-plane orientations ϕ) and rotational constraints under the aforementioned SNR using the Tri-spot PSF. (c)-(e) The distribution of rotational constraint estimations for molecules with average orientations along the x-axis and ground-truth rotational constraints γ_{2D} of (c) 0, (d) 0.1, (e) 0.2 (vertical lines in (c)-(e) and crosses in (b)), respectively.

rotational constraint estimation. The in-plane excitation modulation method has a small bias under a low SNR scenario. However, due to the difference between γ_{2D} and γ_{3D}, the results are not directly comparable with the other methods. The standard PSF and Tri-spot PSF both measure the 3D rotational constraint γ_{3D}. The bias analysis suggests that the Tri-spot PSF is a more accurate method to measure the rotational dynamics of fluorescent molecules.

ACKNOWLEDGMENTS

Research reported in this publication was supported by the National Science Foundation under grant number ECCS-1653777 and by the National Institute of General Medical Sciences of the National Institutes of Health under grant number R35GM124858.

REFERENCES

[1] Moerner, W. E. and Kador, L., "Optical detection and spectroscopy of single molecules in a solid," *Physical Review Letters* **62**(21), 2535–2538 (1989).

[2] Ha, T., Enderle, T., Chemla, D. S., Selvin, P. R., and Weiss, S., "Single Molecule Dynamics Studied by Polarization Modulation," *Physical Review Letters* **77**(19), 3979–3982 (1996).

[3] Ha, T., Glass, J., Enderle, T., Chemla, D. S., and Weiss, S., "Hindered Rotational Diffusion and Rotational Jumps of Single Molecules," *Physical Review Letters* **80**(10), 2093–2096 (1998).

[4] Backer, A. S., Lee, M. Y., and Moerner, W. E., "Enhanced DNA imaging using super-resolution microscopy and simultaneous single-molecule orientation measurements," *Optica* **3**(6), 659 (2016).

[5] Sosa, H., Peterman, E. J. G., Moerner, W. E., and Goldstein, L. S. B., "ADP-induced rocking of the kinesin motor domain revealed by single-molecule fluorescence polarization microscopy," *Nature Structural Biology* **8**(6), 540–544 (2001).

[6] Peterman, E. J., Sosa, H., Goldstein, L. S., and Moerner, W., "Polarized Fluorescence Microscopy of Individual and Many Kinesin Motors Bound to Axonemal Microtubules," *Biophysical Journal* **81**(5), 2851–2863 (2001).

[7] Forkey, J. N., Quinlan, M. E., Alexander Shaw, M., Corrie, J. E. T., and Goldman, Y. E., "Three-dimensional structural dynamics of myosin V by single-molecule fluorescence polarization," *Nature* **422**(6930), 399–404 (2003).

[8] Beausang, J. F., Shroder, D. Y., Nelson, P. C., and Goldman, Y. E., "Tilting and Wobble of Myosin V by High-Speed Single-Molecule Polarized Fluorescence Microscopy," *Biophysical Journal* **104**(6), 1263–1273 (2013).

[9] Lippert, L. G., Dadosh, T., Hadden, J. A., Karnawat, V., Diroll, B. T., Murray, C. B., Holzbaur, E. L. F., Schulten, K., Reck-Peterson, S. L., and Goldman, Y. E., "Angular measurements of the dynein ring reveal a stepping mechanism dependent on a flexible stalk," *Proceedings of the National Academy of Sciences* **114**(23), E4564–E4573 (2017).

[10] Backlund, M. P., Lew, M. D., Backer, A. S., Sahl, S. J., and Moerner, W. E., "The Role of Molecular Dipole Orientation in Single-Molecule Fluorescence Microscopy and Implications for Super-Resolution Imaging," *ChemPhysChem* **15**(4), 587–599 (2014).

[11] Karedla, N., Stein, S. C., Hähnel, D., Gregor, I., Chizhik, A., and Enderlein, J., "Simultaneous Measurement of the Three-Dimensional Orientation of Excitation and Emission Dipoles," *Physical Review Letters* **115**(17), 173002 (2015).

[12] Backer, A. S. and Moerner, W. E., "Extending Single-Molecule Microscopy Using Optical Fourier Processing," *The Journal of Physical Chemistry B* **118**(28), 8313–8329 (2014).

[13] Böhmer, M. and Enderlein, J., "Orientation imaging of single molecules by wide-field epifluorescence microscopy," *Journal of the Optical Society of America B* **20**(3), 554 (2003).

[14] Lieb, M. A., Zavislan, J. M., and Novotny, L., "Single-molecule orientations determined by direct emission pattern imaging," *Journal of the Optical Society of America B* **21**(6), 1210 (2004).

[15] Axelrod, D., "Fluorescence excitation and imaging of single molecules near dielectric-coated and bare surfaces: a theoretical study," *Journal of Microscopy* **247**(2), 147–160 (2012).

[16] Backer, A. S. and Moerner, W. E., "Determining the rotational mobility of a single molecule from a single image: a numerical study," *Optics Express* **23**(4), 4255 (2015).

[17] Mortensen, K. I., Churchman, L. S., Spudich, J. A., and Flyvbjerg, H., "Optimized localization analysis for single-molecule tracking and super-resolution microscopy," *Nature Methods* **7**(5), 377–381 (2010).

[18] Zhang, O., Lu, J., Ding, T., and Lew, M. D., "Imaging the three-dimensional orientation and rotational mobility of fluorescent emitters using the Tri-spot point spread function," *Applied Physics Letters* **113**(3), 031103 (2018).

[19] Barrett, H. H. and Myers, K. J., [*Foundations of image science*], John Wiley & Sons (2013).